Article



Microtubule polymerization generates microtentacles important in circulating tumor cell invasion

Lucina Kainka, Reza Shaebani, Kathi Kaiser, Jonas Bosche, Ludger Santen, and Franziska Lautenschläger, and Franziska Lautensc

¹Department of Natural Science, Experimental Physics, Saarland University, 66123 Saarbrücken, Germany; ²Department of Natural Science, Theoretical Physics, Saarland University, 66123 Saarbrücken, Germany; and ³Center for Biophysics, Saarland University, 66123 Saarbrücken, Germany

ABSTRACT Circulating tumor cells (CTCs) have crucial roles in the spread of tumors during metastasis. A decisive step is the extravasation of CTCs from the blood stream or lymph system, which depends on the ability of cells to attach to vessel walls. Recent work suggests that such adhesion is facilitated by microtubule (MT)-based membrane protrusions called microtentacles (McTNs). However, how McTNs facilitate such adhesion and how MTs can generate protrusions in CTCs remain unclear. By combining fluorescence recovery after photobleaching experiments and simulations we show that polymerization of MTs provides the main driving force for McTN formation, whereas the contribution of MTs sliding with respect to each other is minimal. Further, the forces exerted on the McTN tip result in curvature, as the MTs are anchored at the other end in the MT organizing center. When approaching vessel walls, McTN curvature is additionally influenced by the adhesion strength between the McTN and wall. Moreover, increasing McTN length, reducing its bending rigidity, or strengthening adhesion enhances the cell-wall contact area and, thus, promotes cell attachment to vessel walls. Our results demonstrate a link between the formation and function of McTNs, which may provide new insight into metastatic cancer diagnosis and therapy.

SIGNIFICANCE Microtentacles are microtubule-based membrane protrusions that promote adhesion and extravasation of circulating tumor cells from the bloodstream. Here, we provide the first evidence that microtentacle formation is driven by the polymerization of microtubules against the cell membrane and not by microtubule sliding driven by molecular motors. Polymerization of microtubules anchored to the microtubule organizing center (MTOC), as in the case of microtentacles, induces bending, which results in curved microtentacles. We show that this curvature is relevant for CTC adhesion because it increases the contact area between microtentacles and blood vessel walls.

INTRODUCTION

Circulating tumor cells (CTCs) have attracted widespread attention over the last decade due to their function as seeds for metastasis (1–6). CTCs are transported through the bloodstream (7–9), where they are at high risk of death by apoptosis fragmentation in narrow capillaries, or for recognition by the immune surveillance system. Consequently,

Submitted December 10, 2024, and accepted for publication May 16, 2025. *Correspondence: l.santen@mx.uni-saarland.de or f.lautenschlaeger@

*Correspondence: l.santen@mx.uni-saarland.de or f.lautenschla physik.uni-saarland.de

Lucina Kainka and Reza Shaebani contributed equally to this work. Ludger Santen and Franziska Lautenschläger contributed equally to this work.

Editor: Padmini Rangamani.

https://doi.org/10.1016/j.bpj.2025.05.018

 $\ensuremath{\mathbb{O}}$ 2025 The Author(s). Published by Elsevier Inc. on behalf of Biophysical Society.

This is an open access article under the CC BY-NC license (http://creativecommons.org/licenses/by-nc/4.0/).

thin microtubule (MT)-based membrane protrusions known as microtentacles (McTNs), as shown for mammary epithelial cells (13). While McTNs promote tumor cell reattachment to other cells, extracellular matrix, or endothelial monolayers (13–17), only indirect evidence exists of McTNs facilitating adhesion to blood vessels (18). Thus, little is known about the mechanism underlying tumor cell adhesion to vessel walls and the role McTNs play in this process. In general, membrane protrusions play key roles

less than 1% of CTCs survive and leave the blood system (10,11). The exact mechanism of CTC extravasation is not

yet understood, although adhering to blood vessel walls is

the first crucial step (12). CTCs can generate long and

in processes such as cell migration (19–22), signal conduc-

tion (23, 24), and environmental sensing (25, 26). Most



protrusions are actin- (22,27,28) or MT-based (13,29,30) and the required forces to deform the membrane are generated by either polymerization dynamics (31,32) or sliding of filaments with respect to each other powered by molecular motors (33,34). Polymerization of actin filaments contributes to the development of diverse types of cell protrusions including lamellipodia, filopodia, and invadosomes (27,28). Sliding of MTs by means of molecular motors facilitates processes such as neurite outgrowth (30), axonal regeneration (35), and formation of proplatelets (29). Previous studies suggest that MT polymerization can also contribute to protrusion formation (36–39). To gain insight into how McTN formation in CTCs can be controlled, prevented, or reversed, a detailed understanding of the mechanism driving McTN formation is crucial. Here, we define the dominant mechanism of McTN formation and suggest a mechanism how these long, curved protrusions may enhance cell adhesion to vessel walls.

MATERIALS AND METHODS

Cell culture

Immortalized retinal pigmented epithelium (hTERT-RPE-1) cells were cultured in Dulbecco's modified Eagle's medium/F12 (Thermo Fisher Scientific, Waltham, MA, USA) with 10% fetal bovine serum (Thermo Fisher Scientific, Waltham, MA, USA), 1% GlutaMAX (Thermo Fisher Scientific, Waltham, MA, USA), and 1% penicillin/streptomycin (Thermo Fisher Scientific, Waltham, MA, USA) at 37°C and 5% CO₂. MT dynamics were studied using RPE-1 cells that stably expressed mEmerald-vimentin and TagRFPtubulin, which were kindly provided by Gaudenz Danuser (UT Southwestern, Dallas, TX). EB3 experiments were performed using RPE-1 cells that were transiently transfected with an EB3-tdTomato plasmid. The plasmid was kindly provided by Kristian Franze (Institute for Medical Physics, Friedrich-Alexander-Universität Erlangen-Nürnberg, Erlangen, Germany). Transfection was performed using X-tremeGENE 9 DNA (Merck, Darmstadt, Deutschland) as the transfection reagent, and 200 µg/mL G418 (Merck, Darmstadt, Deutschland) was employed for selection purposes. Following a 2-week selection period, over 90% of cells displayed fluorescence, which persisted for several weeks.

Generation of McTNs

To generate McTNs in RPE-1 cells, cells were detached from the surface using trypsin, centrifuged at 1300 rpm for 3 min, and then resuspended in medium containing 1 μ M latrunculin A (Sigma-Aldrich) and 5 mM HEPES (Gibco). This treatment leads to formation of McTNs within 10 min and is reversible by washout of latrunclin A. To prevent displacement of McTNs during imaging, glass-bottomed microscopy dishes (FluoroDish Cell Culture Dish, FD35-100, WPI Europe) were prepared. The dishes were coated with Cell Tak (Corning Cell-Tak Cell and Tissue Adhesive, Merck), which was diluted in 0.1 M sodium bicarbonate. Each sample was imaged for a maximum duration of 1 h.

Cell adhesion measurement

The experiment was carried out using either untreated RPE-1 cells or RPE-1 cells treated with 1 μ M latrunculin A to induce McTN formation. Throughout all incubation periods, cells were maintained at 37°C with 5% CO₂. Suspended RPE-1 cells (100,000 cells per well) were placed into each well. Medium was changed at intervals of 20, 40, 60, or 90 min to remove unattached cells. After 90 min, cells were incubated for an additional 4 h. The number of attached cells was determined using an MTT assay (Sigma). The cell medium was replaced with an MTT medium solution at a concentration of 0.5 mg/mL and incubated for 40 min. Following this incubation, the MTT solution was replaced with DMSO to dissolve the MTT crystals. The cell number correlates with the intensity of the MTT color, which was measured using a Tecan plate reader. Each well was measured three times, and the mean value was taken. Furthermore, three to four samples per condition were measured and the experiment was repeated on three different days. All values were normalized to the intensity value of a reference for the respective condition well in which cells adhered for 5 h and 30 min. Due to small variance in the exact initial cell number and the number of attached cells, relative values bigger than 1 are possible.

Microscopy

All experiments were performed using a spinning disk unit (CSU W1; Yokogawa, Andor Technology, Belfast, UK) with a pinhole size of 25 μm, coupled to an inverted microscope (Eclipse Ti-E; Nikon, Tokyo, Japan). Images were recorded using a digital camera with a 6.5 μ m pixel size (flash 4.0; Hamamatsu, Hamamatsu City, Japan). Samples were visualized with an oil immersion objective with $60\times$ magnification and a numerical aperture of 1.4. A temperature of 37°C was maintained throughout the experiments using a heating unit (Okolab). HEPES (25 mM) (Gibco) was added to cell culture medium during the experiment to stabilize the pH value.

Image processing

We developed a C++-based package for image processing which enabled extraction of structural characteristics such as length and curvature of the McTNs. The procedure started with reconstruction of the three-dimensional shape of the cells from the successive images taken at different heights. The three-dimensional cell shape is required to correctly track the variations in the curvature and thickness of each McTN and to monitor McTN dynamics and assign an accurate length to them. By combining various existing imageprocessing approaches, we developed a new framework for distinguishing the McTNs from the cell body. By calculating the directional density correlations from the pixel intensity information, we found that the anisotropic decay of the correlations differs greatly between the McTNs and the cell body; as a result, it is possible to decompose the cells into the main cell body and the McTNs. In addition to determining the cell-body boundary and the outline of the entire cells, assigning a length to a curved tube with varying thickness is also a challenging task. The details of our image-processing technique will be published elsewhere. Using the package developed, we can: 1) estimate the McTN length by finding the shortest path along the protrusion body to reach the McTN tip from the nearest cell-body boundary point, 2) estimate the number of McTNs and their total lengths, 3) quantify other morphological properties of interest, including variations in curvature and thickness of the McTN, and 4) track the dynamics of the McTNs by following the time-lapse images, e.g., during the growth of the McTNs.

EB3 experiments

To generate McTNs, cells were prepared as described in generation of McTNs. Time-lapse images were captured from various cells, with the time intervals and overall duration varying across experiments. Experiments were performed on three different days. For analysis, the McTN of interest was traced in Fiji by drawing a segmented line along the McTN. The line originated from the onset of the McTN at the cell body and extended toward the tip of the McTN. In cases where the distance of the McTN tip changed during the time lapse, the maximum distance was recorded. The line thickness was set to 9 pixels, which corresponds to an average McTN thickness of 0.99 µm. A kymograph was generated along this line, representing the mean intensity in the transverse direction of the line. The kymographs were manually analyzed to determine the frequency of MTs entering the McTNs, as well as the frequency of rescue and catastrophe events. To accomplish this, we counted the occurrences of EB3 tips appearing from the McTN base, appearing along the McTN, or disappearing. These counts were then divided by the duration of the experiment and the estimated number of MTs within the McTNs, which we approximated as 10. To analyze the velocities, we used the Kymobutler software which detects tracks within kymographs and calculates several parameters such as the velocities (40). The shown velocities are the mean frame to frame velocities.

FRAP experiment

To generate McTNs, the cells were prepared following the previously described method. To modify the relative contribution of MT sliding, cells were additionally treated with either 5 μ M paclitaxel (Sigma) or 100 μ M kinesore (Sigma). For bleaching, a laser with a wavelength of 561 nm and 70% of maximum power (70 mW/mm²) was used. The bleaching area consisted of a 1 \times 1 μ m square and was manually located approximately at half the length of the McTN length. During image acquisition, a laser with a wavelength of 561 nm and 25% of the maximum power was employed, with an exposure time of 200 ms. The videos consistently followed the same sequence, with images taken at intervals of 500 ms. Image acquisition began 5 s before the bleaching pulse, which lasted for $100 \, \text{ms.}$ Subsequently, images were acquired for a duration of $600 \, \text{s.}$ Throughout the experiment, the Nikon Perfect Focus System was enabled to prevent focus drift. For each condition, 23-24 videos were acquired over the course of different days. The videos were analyzed using a custom MATLAB script following the protocol outlined by Fritzsche and Charras (41). In summary, the intensity values were corrected for background signal and unintentional photobleaching. Square regions of interest (ROIs) were manually selected for ROI1, ROI*, and ROI2 to cover 1 μ m of the McTN (see Fig. S4). The mean intensity within these regions was measured over time. To normalize the intensities, the values in all three ROIs were divided by the respective mean intensity within the first 5 s before the bleaching pulse. In ROI*, the intensity immediately after the bleaching pulse was set to zero as a reference point. Bar plots were generated by first calculating the mean intensity across all experiments within a specific condition. Subsequently, the mean intensities were determined for the following time intervals: t = [0, 60s], t = [0, 300 s], and t = [0, 600 s]. These choices enabled us to compare the cumulative changes of intensity after short, intermediate, and long times.

Statistical analysis and graphical representation

All experimental graphs were generated using the Seaborn library in Python 3. In the bar plots, the box represents the mean value, while the error bars indicate the standard deviation. For the boxplots, the line within the box represents the median value, and outliers are excluded from the visualization. Statistical analyses were conducted using the SciPy library in Python 3. A t-test (ttest_ind) was applied unless the data did not meet the assumption of normality, in which case a Mann-Whitney U-test (mannwhitneyu) was performed. Data were checked for normality by conducting the Shapiro-Wilk test in Python 3. The p values for all statistical tests are provided in the supporting material.

Modeling MT growth against soft barriers

We considered a two-state model for MT dynamics and growth against a soft barrier (42–44), with MT filaments being linear rigid rods consisting of subunits $\delta \simeq 0.6$ nm. The MT tip dynamics was described by four param-

TABLE 1 Parameters describing MT dynamics

Parameter	Value
Force-free polymerization velocity v_G^0	$0.25~\mu {\rm m~s^{-1}}$
Depolymerization velocity v_S^0	$0.4~\mu {\rm m~s^{-1}}$
Force-free catastrophe frequency v_C^0	0.004 s^{-1}
Rescue frequency ν_R	0.0005 s^{-1}

eters: growth r_G and shrinkage r_S rates and catastrophe ν_C and rescue ν_R frequencies. All parameters were extracted from our experimental EB3 and MT kymographs and are summarized in Table 1. By dividing the velocity by the length of one subunit $\delta \simeq 0.6$ nm and taking the inverse, we obtain the corresponding rates.

We used a piecewise linear deformation-force model (depicted in Fig. 4 A), where the force linearly grows with the membrane displacement for small deformations compared with the cell size, but eventually reaches an asymptotic level \mathcal{F} for longer deformations (45-47). According to the Brownian ratchet model (31,48,49), the polymerization rate decays with the force exerted on the tip of a MT of length d as

$$r_G(d) = r_G^0 \exp\left[-\frac{\delta}{k_B T} F(d)\right], \tag{1}$$

where r_G^0 is the polymerization rate of a freely growing MT, k_B the Boltzmann constant, and T the temperature. The asymptotic polymerization rate is given by $r_G^{\infty} = r_G^0 \exp[-\mathcal{F}\delta/k_B T]$. As well as limiting the rate of tubulin addition, the force also reduces the mean time interval τ_{C} between successive catastrophe events, as $au_C(d) = au_C^0 - rac{r_0^0 - r_G(d)}{r_0^0 - r_G^\infty} (au_C^0 - au_C^0)$

 τ_C^{∞}), where τ_C^0 and τ_C^{∞} are the force-free and asymptotic time intervals between the catastrophe events, respectively (50). It was argued in (50) that the pushing force generated by a growing MT against a cellular object regulates the catastrophe time by modifying the rate of GTP-bound tubulin subunit addition. As a result, the catastrophe frequency grows as

$$\nu_C(d) = \frac{\nu_C^0}{1 - \frac{r_G^0 - r_G(d)}{r_G^0 - r_G^\infty} \left(1 - \frac{\nu_C^0}{\nu_C^\infty}\right)},\tag{2}$$

where $\nu_C^0=1/\tau_C^0$ and $\nu_C^\infty=1/\tau_C^\infty$. The above relation can be written as $\nu_C(d)=1/(a+r_G(d))$, which is structurally similar to $\nu_C(d) = d/(a+b r_G)$ proposed in (51). However, the latter explicitly introduces a linear dependence on MT length d, whereas our formulation incorporates an implicit length dependence through the exponential decay of $r_G(d)$ with F(d). We also introduce $p^+(d,t)$ and $p^-(d,t)$ as the probabilities of having a filament of length d at time t in the growing or shrinking state, respectively. The evolution of these probabilities can be described by the following master equations:

$$\begin{cases}
\dot{p}^{+}(d,t) &= r_{G}(d-1) p_{+}(d-1,t) - r_{G}(d)p^{+}(d,t) \\
 &+ \nu_{R} p^{-}(d,t) - \nu_{C}(d) p^{+}(d,t), \\
\dot{p}^{-}(d,t) &= r_{S} p^{-}(d+1,t) - r_{S} p^{-}(d,t) \\
 &+ \nu_{C}(d) p^{+}(d,t) \\
 &- \nu_{R} p^{-}(d,t).
\end{cases}$$
(3)

To demonstrate the evolution of the MT length, these equations were solved by considering the appropriate boundary conditions. For example, a nucleation rate, or alternatively, an instantaneous rescue event, can be defined to prevent shrinkage below d = 0 (i.e., reflecting boundary conditions); in the latter case, the following constraints were imposed

$$\begin{cases}
\dot{p}^{+}(0,t) = r_{S} p^{-}(1,t) - r_{G}(0) p^{+}(0,t), \\
p^{-}(0,t) = 0.
\end{cases}$$
(4)

Similarly, to take into account the limited stretchability of the cell surface, an upper filament length threshold can be imposed by an instantaneous catastrophe event at $d = d_{max}$, which leads to

$$\begin{cases}
\dot{p}^{-}(d_{max}, t) = r_{G}(d_{max} - 1) p^{+}(d_{max} - 1, t) \\
-r_{S} p^{-}(d_{max}, t), \\
p^{+}(d_{max}, t) = 0.
\end{cases} (5)$$

By setting all time derivatives to zero, the probability distribution of the filament length in the steady state can be deduced (52). We numerically obtained the stationary distribution of the MT length $p(d) = p^+(d) + p^-(d)$ and, thus, the probability distribution of the protrusion length $P(\ell)$ in terms of the asymptotic force \mathcal{F} .

Modeling semiflexible filaments

To model semiflexible McTNs, we considered a filament of total length Ldivided into n+1 segments with length $l=\frac{L}{n+1}$. Thus, the centerline of the filament was segmented into n + 1 edges $\mathbf{x}_0, \mathbf{x}_1, ..., \mathbf{x}_n$. The elastic energy E of the filament consists of bending E_{bend} and extensional E_{ext} energy terms (53). Using $\mathbf{e}_i = \mathbf{x}_{i+1} - \mathbf{x}_i$ and introducing curvature $\kappa_i =$ $2 \tan \frac{\phi_i}{2} (\phi_i \text{ being the turning angle between two consecutive edges}), the$ bending energy term is given by (54)

$$E_{bend} = YI \sum_{i=1}^{n-2} \frac{(\kappa \mathbf{b})_i^2}{l}, \tag{6}$$

with Y being the Young's modulus, I the moment of inertia of each segment, and $(\kappa \mathbf{b})_i$ the discrete curvature binormal defined as $(\kappa \mathbf{b})_i = \frac{2 \mathbf{e}_{i-1} \times \mathbf{e}_i}{l^2 + \mathbf{e}_{i-1} \cdot \mathbf{e}_i}$. To conserve the overall length of the filament, we employed an extensional en-

$$E_{ext} = \frac{YA}{2} \sum_{i=0}^{n-2} \left(\frac{\|e_i\|}{l} - 1 \right)^2, \tag{7}$$

with A being the cross section of the filament. The total energy of the filament was obtained by adding the contribution of the adhesion energy (introduced in the main text) to the bending and extensional energies. Finally, by minimizing the total energy, the optimal configuration of the filament was obtained. Original data are available at: https://doi.org/10.6084/m9.figshare. 27021139.v1.

RESULTS

Generation of McTNs in noncancerous RPE-1 cells

To determine the driving mechanism of McTN formation, specifically whether McTNs arise from MT polymerization or sliding (Fig. 1 B), we first identified a sufficient model cell line. We hypothesized that the mechanism of McTN formation is independent of the cancerous phenotype of the cell, as sufficient weakening of the actin cortex of any cell is the major underlying mechanism (57). Previously, McTN formation was found to be induced or enhanced by destabilization of the actin cortex with drugs such as latrunculin A (13). Thus, latrunculin A treatment of suspended RPE-1 cells, which endogenously express TagRFP-tubulin, results in the formation of membrane protrusions filled with MTs (Fig. 1 A, more exemplary images of RPE-1 cells in Fig. S1 A). Moreover, these protrusions phenomenologically resemble McTNs shown in literature (Fig. 1, C–E). These latrunculin A-induced membrane protrusions grow within 15 min, as reported by Killilea et al. (58), and persist for hours. Three random RPE-1 cells were selected at 15 min after latrunculin A treatment and the lengths of all of their three-dimensional protrusions were measured over a period of 80-120 min. For each cell and each time point the mean length of all protrusions was determined. To compare the length dynamics of these three cells, we normalized the protrusion length by dividing by the mean length during the first 60 min. Our data show that, despite minor fluctuations, the latrunculin A-induced protrusions continue to grow for roughly an hour after their initial formation (in the first 10 min), and then reach a steady state (Fig. 1 G, see Fig. S1 B for absolute McTN lengths). Consequently, although these protrusions consist of a MT bundle, they do not exhibit the dynamic instability typically expected of individual MTs. Since McTNs promote the reattachment of cells (13), we checked whether latrunculin A-induced protrusions formed by RPE-1 cells fulfill this same function. Treated or untreated RPE-1 cells were plated in suspension. To quantify cell attachment within a given time, cell media were exchanged after 20, 40, 60, and 90 min. Cells that had already attached remained in the dish and were counted. At shorter time points, a higher amount of treated RPE-1 cells with MT-based protrusions attached to the surface than did untreated cells. The relative difference of attached cells decreased with time but was still clearly visible after 90 min (Fig. 1 H). This clearly shows that latrunculin A-induced protrusions in RPE-1 cells promote reattachment of these cells. Furthermore, as depolymerization of actin enhances adhesion, the mechanism appears to be independent of f-actin (18). Experiments were then repeated on surfaces with different coatings: a Pll-g-PEG coating is commonly used to decrease adhesiveness of a surface and a fibronectin coating enhances focal adhesion and thus actin-based adhesion. While untreated RPE-1 cells clearly adhere best on a fibronectin-coated surface, adhesion of cells with latrunculin A-induced protrusions was independent of the coating (Fig. S1 C). This confirms that the adhesion mechanism of RPE-1 cells with latrunculin A-induced protrusions is independent of Interestingly, RPE-1 cells with latrunculin A-induced protrusions also partly adhere to Pll-g-PEGcoated surfaces. Due to the current lack of data on McTNs generated by patient-derived CTCs, it is not possible to compare values such as length or number of McTNs of RPE-1 cells with patient-derived CTCs. However, due to the similarity of latrunuculin A-induced protrusions to McTNs and their ability to promote adhesion in

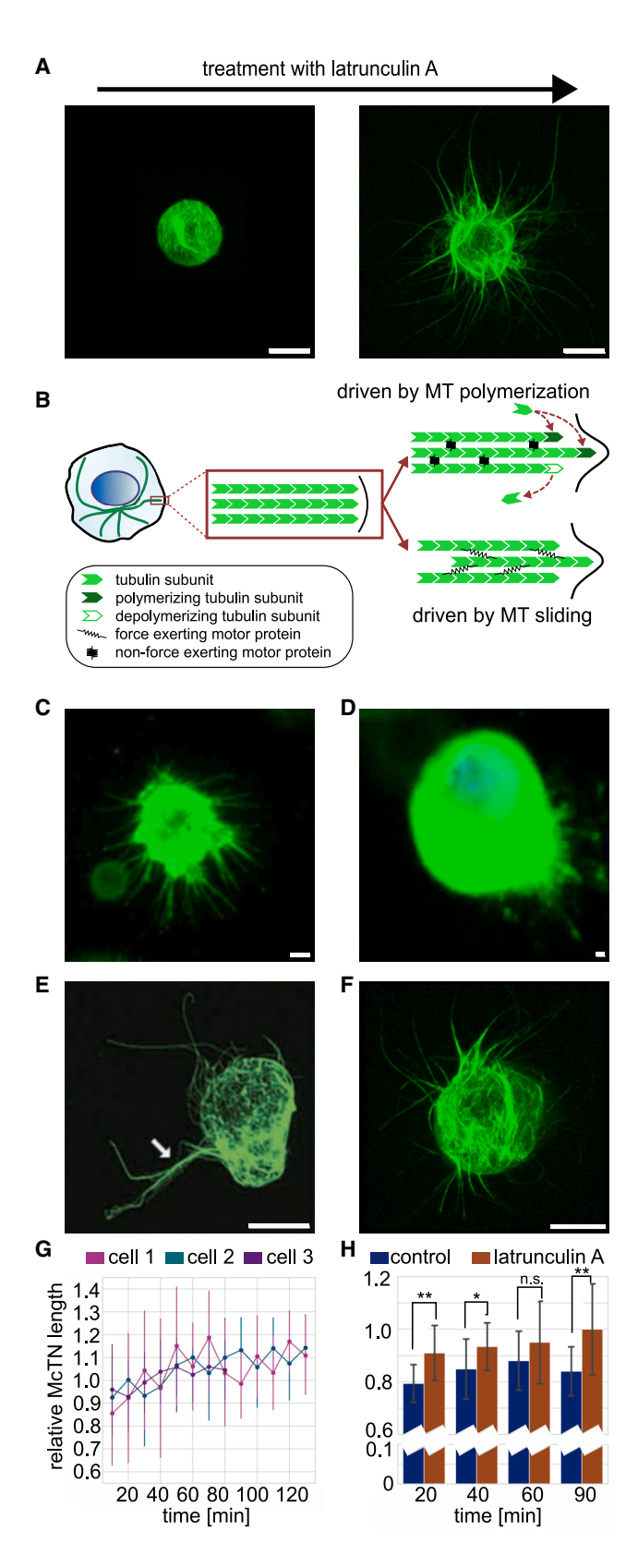


FIGURE 1 Microtentacles in CTCs and RPE-1 cells. (A) Representative images of RPE-1 with MTs stained in. Treatment of detached noncancerous RPE-1 cells with latrunculin A, an inhibitor of actin polymerization, generates McTNs. Scale bars, 10 μ m. (B) Schematic representation of possible

an f-actin-independent mechanism, we conclude that the protrusions formed by RPE-1 cells are McTNs. This further demonstrates that the mechanism of McTN formation is valid beyond the context of cancer cells. We therefore continued our study using RPE-1 cells.

McTNs consist of a bundle of parallel MTs anchored in the MT organizing center

Since McTNs are MT-based membrane protrusions, we asked whether the organization of MTs in McTNs resembles that in other MT-based protrusions. In neurites or proplatlets, for example, MTs exist in fragmented or bundled states with mixed polarities (59,60,61). When adhered to a substrate, RPE-1 cells have a clearly identifiable MT organizing center (MTOC) from which the majority of MTs emerge (Fig. S2 A). However, detachment from substrate could alter the organization of MTs. Due to the high MT density in suspended cells, it is challenging to identify individual MTs inside the cell body and trace them back to the MTOC. Tracking of individual plus-end binding proteins EB3 from within the cell body to the McTN tip was also not possible due to the high MT density with different orientations. However, inside McTNs, MTs polymerize in a parallel way and we could determine MT polymerization dynamics and orientation inside McTNs by tracking EB3 tracks. MTs display dynamic instability, which means that they constantly change between a growing and a shrinking state. Changing from the growing to the shrinking state is termed catastrophe and switching from the shrinking to the growing state is termed rescue (42). To study MT polymerization dynamics, RPE-1 cells were transfected with a plasmid for EB3-RFP, a fluorescent protein that binds to the growing plus-ends of MTs. All experiments were performed 15 min after latrunculin A treatment, and a sample was imaged for a maximum of 1 h to have McTNs in a stable

mechanisms of MT-based protrusion formation at the cell membrane. This process can be driven by MT polymerization dynamics or by sliding of MTs against each other powered by molecular motors. (C-F) McTNs have different shapes, numbers, and lengths depending on the cellular system. Scale bars, 10 μ m. (C) McTNs in the CTC cell line CTC-MCC-41. Membrane stained with WGA. Image taken from (56). (D) McTNs formed by a CTC of a TNBC patient. Membrane stained with WGA. Image taken from (56). (E) McTNs formed by a cancer HCC1428 cell. α-Tubulin staining. Image taken from (16). (F) McTNs formed by a noncancer RPE-1 cell, α-tubulin staining. (G) McTN length over a time course of 80–120 min of three randomly chosen cells. For each cell and each time point, mean length of all McTNs was determined. Values were normalized by the mean length measured during the first 60 min (error bars show standard deviation.). (H) McTNs improve cell attachment. The relative number of attached cells increases over time of McTN generation. Data collected at 20, 40, 60, and 90 min. Untreated cells (blue bars) are compared with cells treated with 1 μM latrunculin A (red bars) to induce McTN formation. The relative number of attached cells was determined with MTT assay. Attached cells after 5 h 30 min serve as a reference value. *** $p \le 0.001$, ** $p \le 0.01$, * $p \le 0.05$; n.s., not significant; Mann-Whitney U-test, $n \ge 6$. Error bars show standard deviation.

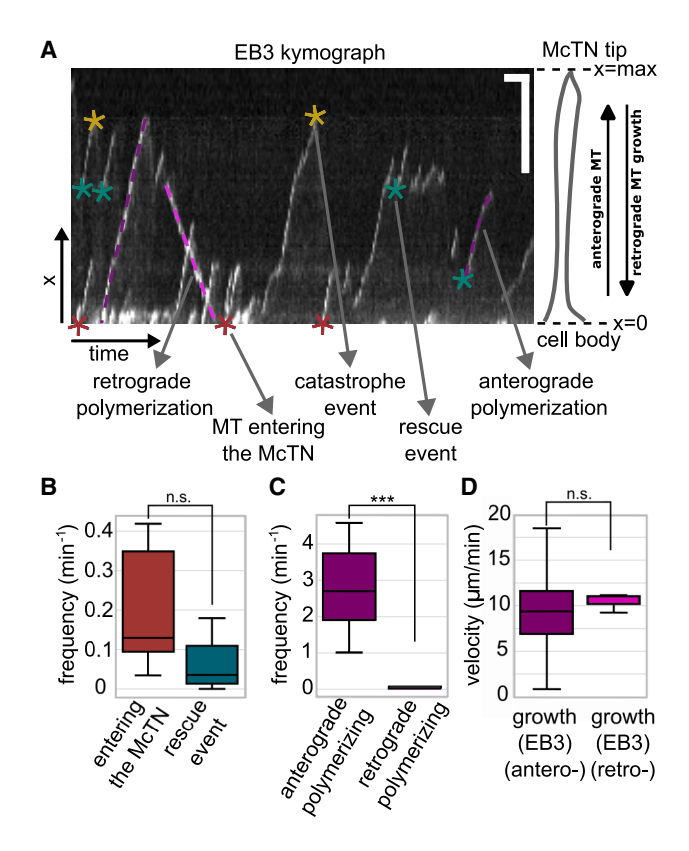


FIGURE 2 MT dynamics within McTNs. (A) Exemplary kymograph of MT plus-end binding protein EB3 within a McTN. Different colors mark examples of different dynamic events, such as anterograde (dark purple lines) and retrograde (light magenta line) polymerization, rescue (blue stars), and catastrophe (yellow stars) events, and new MTs entering the McTN from the cell body (red stars). Scale bars, time, 60 s; space, 5 μ m. (B) Frequencies of MTs entering the McTN and rescue events (N=16). (C) Frequencies of anterograde and retrograde polymerizing EB3 comets (N=16). (D) Anterograde and retrograde polymerization velocities from EB3 kymographs (N=35). *** $p \le 0.001$; n.s., not significant (Mann-Whitney U-test). Horizontal lines of boxplot indicate the median, the boxes represent the interquartile range (IQR, 25th to 75th percentile and whiskers extend to $1.5 \times IGR$. Outliers not shown.)

or slightly growing phase (see Fig. 1 G). Time-lapse images of cells with observable EB3 signal within McTNs were acquired (Video S1) and kymographs were generated (Fig. 2 A). From the kymographs, we quantified the appearance and disappearance of EB3 signals. Disappearance of an EB3 signal corresponds to a catastrophe event. Appearance of EB3 signals corresponds to either a rescue event within the McTN or, if the EB3 track appears at the base of the McTN, it is a new MT polymerizing into the McTN (Fig. 2 A). To calculate the corresponding frequencies, we normalize the number of events by the number of MTs inside the McTN. This has been described before as 9–13 MTs per McTNs (58). We therefore assumed bundles of 10 MTs in each McTN and used this value to determine the frequencies of new MTs entering the McTN, rescue events (Fig. 2 B), and catastrophe events (Fig. S6 C). We find that most EB3 signals originated from within the cell body (Fig. 2 B) and polymerize toward the McTN tip (anterograde) (Fig. 2 C). This suggests that McTNs mainly consist of parallel MT bundles. Only rarely did EB3 tracks move toward the cell body (retrograde) (Fig. 2 C). To confirm that this is a result of retrograde polymerization, we compared the velocities of anterograde and retrograde moving EB3 tracks and found no significant difference (Fig. 2 D). We assume that retrograde polymerization events result from spontaneous nucleation events. Nevertheless, such nucleation events are very rare. This is further supported by scanning electron images which only show continuous MTs emerging from within the cell body (Fig. S3). We conclude that, inside McTNs, the majority of MTs have their plusends facing the McTN tip, they originate from the cell body, and that they are likely connected to the MTOC. Super-resolution imaging by Killilea et al. led to the same conclusion (58). Moreover, such connection to the MTOC potentially serves as a stabilizing point that helps MTs to generate the pushing forces required for protrusion of the cell membrane.

Visualizing MT sliding dynamics through FRAP experiments

As shown above, MTs inside McTNs polymerize; however, an additional sliding mechanism may underlie McTN formation and could be linked to the functional role of McTNs. To address this, we performed fluorescence recovery after photobleaching (FRAP) experiments. A high-intensity laser pulse was directed at a ROI* along the stable McTN, leading to fluorescence loss in the defined ROI* and subsequent intensity recovery (Fig. 3 B; Video S2). ROI* was manually located at approximately the middle of the McTN. The mean intensity within the region was calculated and all values were normalized against the initial mean intensity value (for more details see materials and methods). Due to the observed fast polymerization dynamics of MTs inside McTNs, the recently introduced mathematical approach to study filament transport (62) cannot be applied here. Instead, intensity data were extracted from the ROI* as well as from two adjacent regions: ROI1 (toward the cell body) and ROI2 (toward the McTN tip) (Fig. 3 A). All three regions (ROI*, ROI1, and ROI2) were manually selected to cover approximately 1 μ m of the McTN (exemplary images in Fig. S4). Typically, for FRAP experiments intensity-over-time curves are presented (compare with Fig. 3 C). However, for better visualization of different scenarios, we introduce an alternative representation in which the mean intensity was calculated within a time interval, T, and the intensity at the bleaching time point was subtracted (for more details see materials and methods). This yields a dimensionless quantity which we termed mean intensity change (Fig. 3 D). For scenarios of pure MT polymerization dynamics inside McTNs, we anticipate fluorescence recovery in ROI* due to 1) new MT polymerization

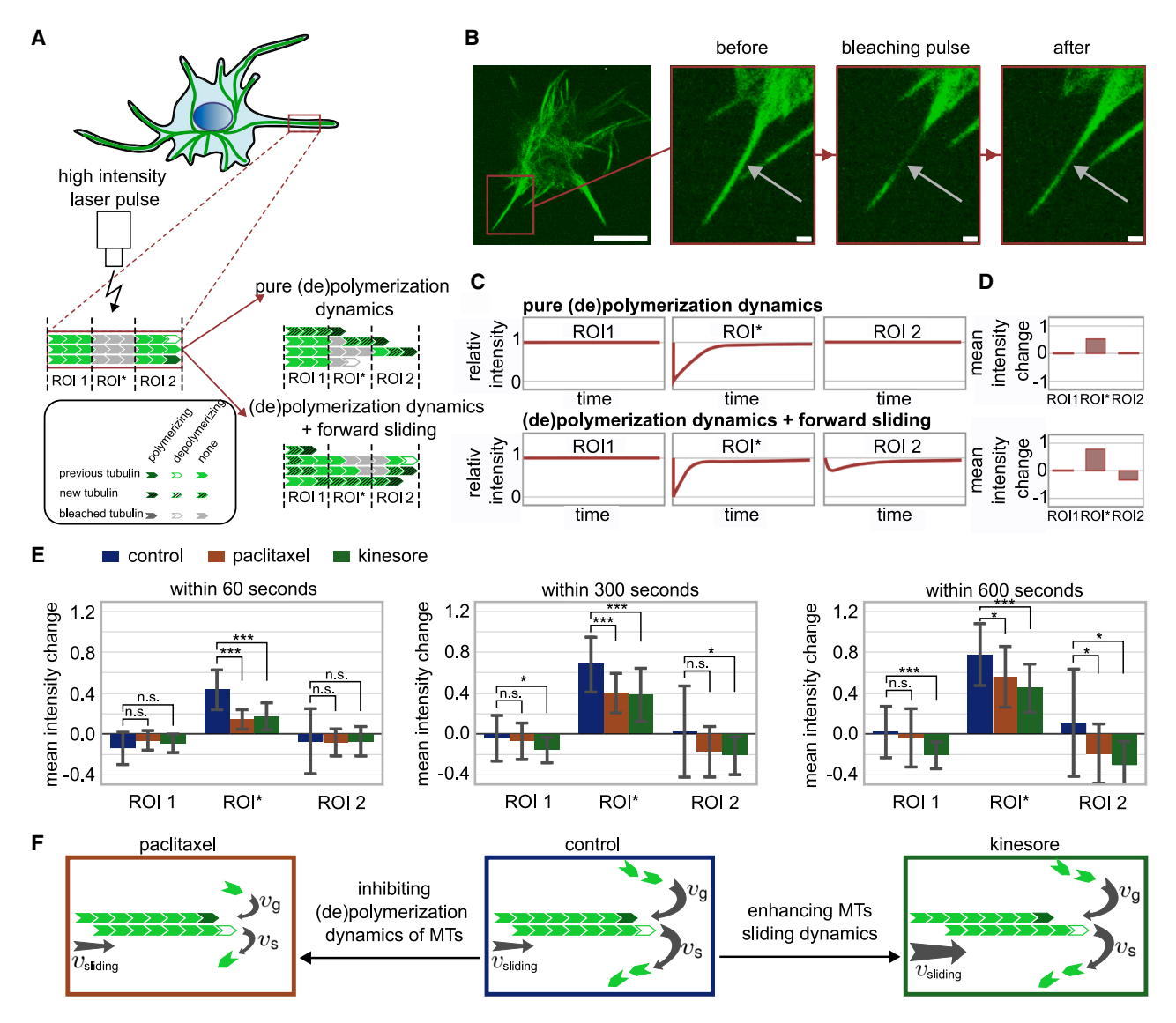


FIGURE 3 Fluorescence intensity recovery after photobleaching (FRAP) experiments. (A) Schematic representation of McTN FRAP experiment. A highintensity laser pulse bleaches the fluorescent MT bundle in a region of interest (ROI*). Two possible scenarios for changes in fluorescence intensity of two adjacent regions (ROI1 and ROI2) are depicted. For pure MT polymerization dynamics, the bleached tubulin subunits cannot enter the ROI1 and ROI2 regions; thus, the intensities of these regions remain unchanged. On the contrary, additional forward sliding dynamics of MTs can push bleached tubulin subunits into ROI2 and reduce intensity. (B) Exemplary images of a bleached region (indicated with arrows) over the course of the experiment. Before applying the bleaching pulse on a selected McTN (marked in the left frame), the entire MT bundle is fluorescent. The bleaching pulse results in a local loss and subsequent recovery of fluorescence over time. Scale bars, 10 μ m (left panel), 1 μ m (rest of the panels). (C) Expected time evolution of fluorescence intensity in ROI*, ROI1, and ROI2 regions for two possible scenarios. (D) Expected mean intensity change within a given time interval with respect to the intensity at the bleaching time point for both scenarios and three different regions of interest. (E) Mean intensity change within first 60, 300, or 600 s with respect to the intensity at the bleaching time in ROI1, ROI*, and ROI2. All cells were treated with 1 μ M latrunculin A. Additionally, 5 μ M paclitaxel or 100 μ M kinesore was used to inhibit MT polymerization or enhance MT sliding, respectively. Number of experiments: control, N = 23 (blue); paclitaxel, N = 23 (brown); kinesore, N = 24 (green). Error bar shows standard deviation. (F) Schematic representation of the impact of paclitaxel and kinesore on MT dynamics. While paclitaxel inhibits MT polymerization, kinesore enhances the sliding dynamics of MTs. *** $p \le 0.001$, ** $p \le 0.01$, * $p \le 0.05$; n.s., not significant (t-tests).

into ROI*, 2) MT depolymerization followed by rescue events in front of ROI* (relative to the cell body), or 3) MT depolymerization with rescue events within ROI* (Fig. 3 A). In these scenarios, the mean intensities in ROI1 and ROI2 remain unchanged (Fig. 3, C and D). Next, we consider the presence of additional sliding dynamics. While it should be noted that retrograde and bidirectional sliding may also occur, to investigate the basic concept we assessed forward (anterograde) sliding. In a mixed polymerization and forward sliding scenario, the fluorescence intensity in ROI2 (or ROI1 in the case of backward sliding) should also be affected. While the recovery of fluorescence intensity in ROI* is accelerated due to fluorescent MTs sliding from ROI1 into ROI*, the intensity in ROI2 decreases because of bleached MTs sliding into ROI2 (Fig. 3, A, C, and D). The relative contribution of sliding and polymerization mechanisms dictates the magnitude of difference between the increase of intensity in ROI* and ROI2. In the extreme case of pure sliding, the increase of intensity in ROI* would equal the decrease of intensity in ROI2. Note, that diffusion of free tubulin can also change the fluorescent intensity. However, the highly confined geometry of McTNs leads to drastically reduced diffusion coefficients compared with diffusion in cytoplasm and is therefore insufficient to affect the observed trends.

MT polymerization dominates over MT sliding dynamics inside McTNs

We performed FRAP experiments using RPE-1 cells expressing TagRFP-tubulin. To induce McTN formation, cells were treated with 1 μ M latrunculin A. RPE-1 cells formed stable McTNs within 15 min. We refer to this condition as the *control*. Since we have no information on the timescale at which MT sliding in could occur in our system, we decided to study the dynamics on different timescales and determined mean intensity changes within time intervals of 60, 300, and 600 s. In control experiments, there is an initial fast recovery in ROI* (40% within 60 s) followed by a slower recovery (80% within 600 s) (Figs. 3 E and S5 A). As explained above, sliding dynamics would manifest in an intensity reduction in one or both regions adjacent to ROI*. While a slight decrease in intensity occurred within the first 60 s in both regions, this effect diminished over time (Fig. 3 E). Importantly, this intensity drop did not exceed the amplitude of intensity fluctuations (Fig. S5 A). We assume that such a slight reduction in intensity is potentially an artifact of the measurement (e.g., a transient enhancement of MT depolymerization caused by the bleaching pulse). Therefore, we interpret our control experiments such that polymerization of MTs has a dominant role. However, we cannot exclude a potential contribution of sliding obscured by the fast polymerization dynamics. To test this, we treated cells with 5 μ M of paclitaxel to inhibit MT polymerization (63) (Fig. 3 F). Our observations in EB3-transfected cells (Video S3) as well as the slower and reduced intensity recovery in ROI* (Fig. 3 E) confirmed this inhibition. While treatment with paclitaxel had no clear influence on the intensity in ROI1, the intensity in ROI2 consistently decreased within 600 s after the bleaching pulse (Fig. 3 E). These results demonstrate that there is an effect of forward sliding dynamics of MTs inside McTNs such that bleached MT subunits slide from ROI* into ROI2, likely due to kinesin-1 activity (30,63). To test this, cells were treated with 100 μ M kinesore, a compound known to enhance kinesin-1 activity by binding to its cargo-binding domain, thus increasing its affinity for adjacent MTs (64) (Fig. 3 F). If kinesin-1 mediates MT sliding dynamics within McTNs, kinesore treatment should increase the contribution of sliding dynamics relative to polymerization dynamics. In fact, following kinesore treatment, the intensity in ROI2 only slightly decreased compared with the paclitaxel condition (not significant, compare p values in supporting material). Instead, the effect of kinesore treatment is more visible in ROI1 where the intensity is significantly decreased compared with control and paclitaxel (*, compare p values in supporting material) conditions. Additionally, upon kinesore treatment intensity recovery in ROI* also slowed down (Fig. 3 E). This is possibly a result of 1) backward sliding and 2) indirect effects of kinesore on MT polymerization dynamics. Taken together, we conclude that, in control cells, MT dynamics inside McTNs are primarily governed by polymerization and the effect of sliding only becomes visible when either MT dynamics or kinesin activity is changed. As further confirmation, we asked whether the additional contribution of sliding is essential for generating the forces required for McTN formation.

MT polymerization drives McTN formation

To disentangle the contributions of different MT dynamics on McTN formation, numerical simulations of MT dynamics and growth against a membrane were performed. The complex structure of MTs was simplified as rods consisting of subunits. The MTs were considered to be either in a growing (polymerization) or shrinking (depolymerization) state (42,43,65,66). In such a two-state model, the dynamics at the MT tip is phenomenologically described by growth and shrinkage velocities as well as catastrophe and rescue frequencies. These parameters were extracted from the EB3 and MT kymographs (Figs. 2 C and S6, B and C) (see materials and methods for master equations describing the time evolution of the MT length). MTs polymerize freely until they reach the cell membrane, which exerts a force on the MT tips. This force depends on properties of the membrane (e.g., bending rigidity and surface tension (47)). Note that the force is nonmonotonic for small deformation but reaches an asymptotic force \mathcal{F} for deformations bigger than 1% (45,46) of the cell radius, which McTNs are (Fig. 4 A). According to the Brownian ratchet model, the force exerted by the membrane affects the growth velocity (31,48,49) and catastrophe rate (50) (see Eqs. 1 and 2 in materials and methods). Since McTNs consist of a bundle of MTs, the force is equally shared between MTs in close vicinity of the cell membrane (67-69). The number of MTs in the bundle affects load sharing at their tips and consequently influences McTN length regulation. As the extraction of MT growth dynamics parameters from EB3 and MT experimental kymographs was based on the assumption of a 10-MT bundle, we maintained the same assumption in our simulations for consistency. We note that our reported trends and conclusions remain robust

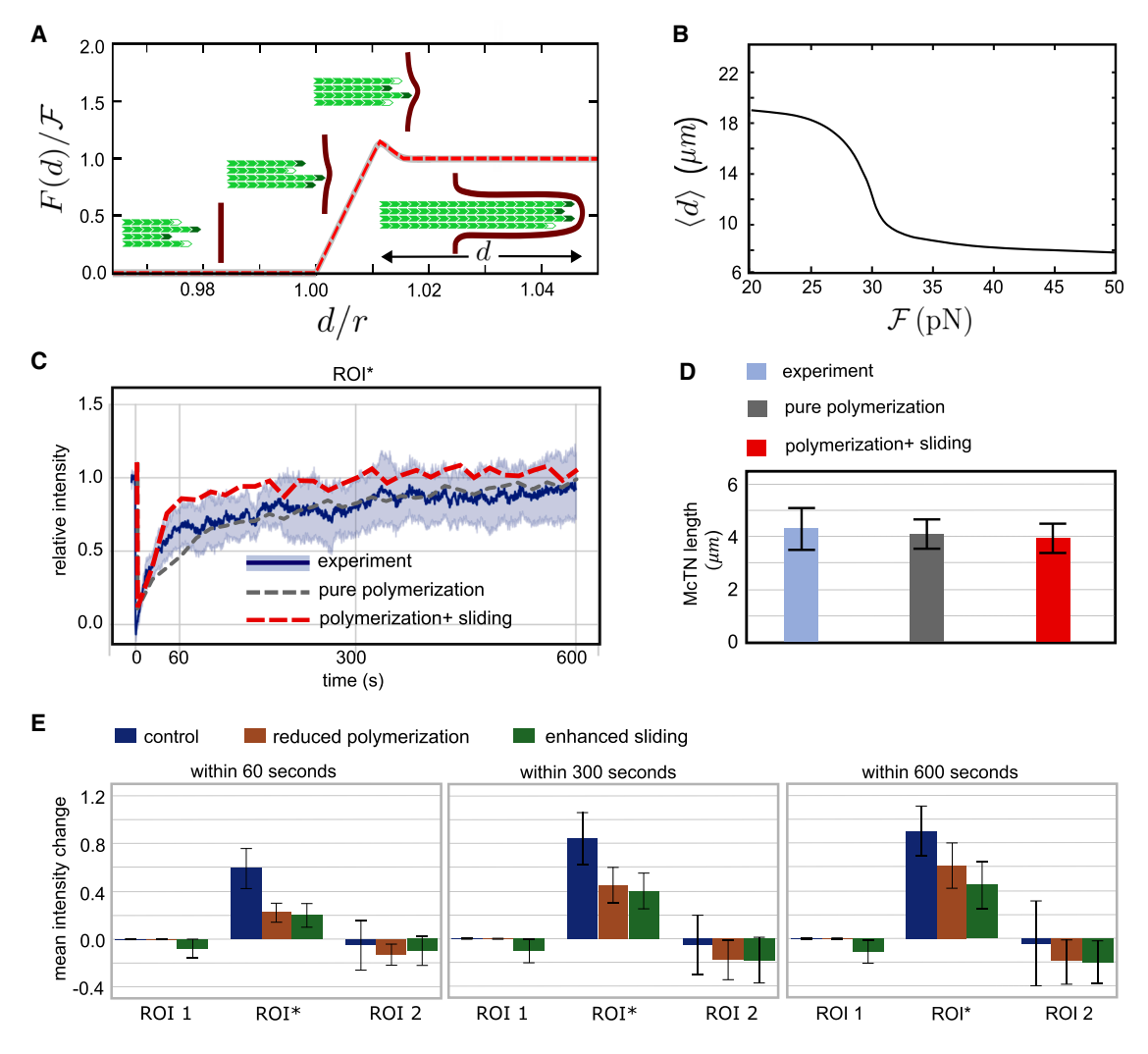


FIGURE 4 MT growth and FRAP simulations. (A) Force exerted on the MT tip (scaled by the asymptotic force \mathcal{F}) versus the MT length d scaled by the cell radius r (solid gray line). The dashed line represents the piecewise linear approximation used in our simulations. Insets are schematics of a MT bundle growing against the barrier in different deformation-force regimes. (B) Mean MT length $\langle d \rangle$ in terms of the asymptotic force \mathcal{F} for a cell of radius 10 μm. (C) Time evolution of the relative intensity in ROI* from control experiments (blue line) and simulations with pure polymerization (gray) or polymerization plus forward sliding dynamics of MTs (red). Shaded region indicates standard deviation of experimental data. (D) Mean McTN length obtained from control experiments, simulations with pure MT polymerization, or simulations with polymerization and sliding dynamics. Error bars show standard deviation. (E) Mean intensity change within first 60, 300, or 600 s in ROI1, ROI*, and ROI2 obtained from control (blue), reduced polymerization (brown), and enhanced sliding (green) simulations. Error bars show standard deviation.

regardless of the chosen number of MTs per McTN. While this choice influences the quantitative results, it does not affect the overall findings. Since in the control condition of our FRAP experiments we could hardly see any sign of MT sliding dynamics, we asked whether a pure polymerization mechanism (i.e., without including the sliding of MTs against each other) could reproduce the length distribution of McTNs obtained in our experiments. From these experiments we obtained the parameters describing MT dynamic instability. However, the force exerted by the membrane on the MT tip is an unknown parameter. Therefore, we calculated the mean McTN length as a function of the force exerted by the membrane (Fig. 4 B). We compared this to the measured length of McTNs and found that a force of $\mathcal{F} \approx 28.7$ pN minimizes the error between simulated and experimental length distribution and fits to the order of magnitude of forces generated in vitro by MT bundles (67). Next, we checked whether we could also reproduce the FRAP experiments with these parameters. To repeat the FRAP experiment numerically, we marked all the MT subunits located in a region of length 1 µm (ROI*) and extracted the time evolution of subunit exchange in this region. Our model with pure polymerization dynamics leads to a slower intensity recovery in ROI* compared with the experiments (Figs. 4 C and S7). The simulation curve has an overall deviation of around 22% from the experimental data. This suggests that MT sliding dynamics is important to reproduce FRAP dynamics. To test this, we included forward sliding dynamics in the simulations by employing a simple model: MTs can randomly switch between sliding and nonsliding mode. As an approximation, the sliding velocity was set as equal to the MT growth velocity (see Table 1). We note that the sliding velocity of MTs relative to each other is governed by the velocity of motor proteins along MTs, which depends on the specific type of motor protein, as well as factors such as ATP concentration and cargo load. Typical velocities range, e.g., from ~ 0.2 to $0.4 \,\mu\text{m/s}$ for kinesin-2 (70) and from 0.4 to 0.8 $\mu\text{m/s}$ for kinesin-1 (71), which are of the same order of magnitude as the polymerization velocity. While some motors can move faster, the MT remains in simultaneous contact with neighboring MTs within the bundle, imposing additional constraints that reduce the sliding velocity. In sliding mode, the MT tips close to the McTN tip exert an additional force on the membrane. We varied this sliding force as a free parameter to reach the best fit to the experimental recovery data (Fig. 4 C). With a sliding force of ~ 3.2 pN, the numerical recovery curve has the minimal overall deviation of only around 5% from the experimental data. We conclude that MT sliding dynamics is needed to describe MT dynamics on the timescale of fluorescent recovery. To further validate our model, we also reproduced paclitaxel and kinesore experiments, as well as the intensity evolution in all three ROIs (see Fig. S7, B and C). By reducing the MT polymerization dynamics or increasing the sliding force in FRAP simulations, the experimental results were reproduced with nearly 10% of relative errors (Figs. 4 E and S7, B and C). By including the forward sliding dynamics into the model we also improved the resulting McTN length statistics compared with the pure polymerization mechanism: the combination of MT polymerization and forward sliding generates McTNs with a mean length of 4.1 \pm 0.6 μ m, comparable with the mean McTN length of 4.3 \pm $0.8 \,\mu\mathrm{m}$ in the control experiments (Fig. 4 D). Pure MT polymerization dynamics produce slightly shorter protrusions, measuring 3.9 \pm 0.6 μ m, although the difference is not statistically significant within the measurement error. The improvement on reproducing McTN length distribution is not as strong as seen for the FRAP curves, which suggests that MT sliding is hardly important to generate McTNs. Importantly, our simulations reveal that the force exerted due to polymerization is an order of magnitude larger than the force generated by sliding.

Kinesore detaches MTs from the MTOC and straightens McTNs

Given the anchorage of MTs in the MTOC and our finding that the forces generated at the McTN tip by polymerization are nearly 10 times larger than those from sliding, it is reasonable to expect that MT polymerization plays a more significant role than sliding in McTN bending. To test this hypothesis, we compared McTN curvature in control cells with those treated with paclitaxel or kinesore. We quantified McTN straightness by calculating the ratio of the Euclidean distance between the McTN base and tip to its actual length. Reducing MT polymerization dynamics in paclitaxeltreated cells (which decreases the McTN tip force) results in straighter McTNs compared with McTNs of control cells (Fig. 5 A). Additionally, McTNs in these cells are slightly shorter due to reduced polymerization. The results for kinesore-treated cells are, however, counterintuitive. One would expect that kinesore treatment increases sliding forces compared with control cells, leading to enhanced McTN bending. Contrary to this expectation, McTNs in kinesoretreated cells are even straighter than in control cells (Fig. 5 A). This can be explained by the loss of MT anchorage at the MTOC following kinesore treatment. In approximately 20% of kinesore-treated cells, we observed clear displacement of the bleached ROI* along the McTN (see, e.g., Fig. 5 B), suggesting reduced anchoring. Such displacement over several microns would be restricted if MTs remained anchored at the MTOC. Furthermore, in adhered kinesore-treated cells, MT organization appeared altered: the MTOC, typically the point of MT emergence, was no longer visible and, instead, MTs accumulated at the cell periphery (Fig. S2 B). The loss of MT anchorage at the MTOC and stronger sliding dynamics in kinesoretreated cells result in longer and straighter McTNs. Additionally, an increased density of kinesin motors has been shown to enhance the MT rescue rate (72), leading to longer MTs and, consequently, longer McTNs. A higher kinesin density also strengthens MT cross-linking within the bundle, increasing McTN rigidity. Furthermore, the force required to buckle a semiflexible filament scales with the square of its cross-sectional area. As a result, the forces acting on the McTN tip in kinesore-treated cells are insufficient to induce buckling, providing another explanation for the observed straightening of McTNs in kinesore-treated

Flexible, long McTNs enhance adhesion of cells to vessel walls

We demonstrated that McTN formation is accompanied by McTN bending due to the forces exerted by the deformed membrane on the McTN tip in the presence of the MTOC. Next, we assessed if both length and bending of McTNs are crucial factors in promoting cell adhesion to blood vessel walls. The McTN was discretized and, for generality, the adhesive interaction between the segments of the McTN and a flat surface was considered nonspecific. The McTNwall interaction was modeled using the Lennard-Jones potential (73) described as $U(r) = 4\epsilon \left[(\sigma/r)^{12} - (\sigma/r)^{6} \right]$. Here, ϵ is the potential well depth (representing the adhesion strength), r the distance between each McTN segment and the surface of the vessel wall, and σ the zero potential distance. Additionally, to take into account the inherent

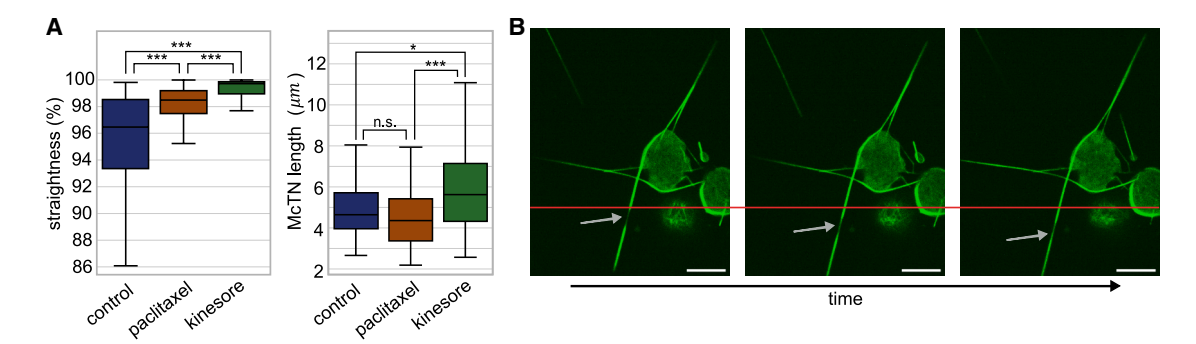


FIGURE 5 Detachment of MTs from the MTOC by kinesore treatment. (A) Straightness of McTNs defined as the end-to-end distance divided by the total length of the McTN (left) and mean length of McTNs (right) under different treatments. *** $p \le 0.001$; n.s., not significant; Mann-Whitney U-test, $n \ge 100$. Horizontal lines of boxplot indicate the median, the boxes represent the interquartile range (IQR, 25th to 75th percentile and whiskers extend to 1.5×IGR. Outliers not shown. (B) Moving of a bleached area (marked with arrows) along the McTN due to sliding of MTs in a kinesore-treated cell. The horizontal red line indicates the initial position of the bleached area. Scale bars, $10 \mu m$.

bending of the McTN, we calculated the elastic energy E of the McTN set by its structure (see materials and methods). The interplay of adhesion and elastic energy determines the overall curvature of the McTN. However, it should be noted that the conclusions in this section remain independent of the choice of adhesive interaction. The extent of cell-wall attachment was characterized by relative wall connection, defined as the fraction of the McTN length closer than a threshold distance to the surface. Since the resulting curvature of the McTN depends on the competition of elastic and adhesion energies, the parameter E/ϵ was added to represent the relative stiffness. By varying the McTN length and E/ϵ , the phase diagram of the relative wall connection was obtained in terms of the McTN length and relative stiffness. While long McTNs with small relative stiffness (i.e., either with a small elastic energy or a strong adhesion strength) show the highest relative wall connection, short McTNs with high relative stiffness have the least connection (Fig. 6 A). Although McTNs of kinesore-treated cells were relatively straighter, kinks were often observed along their length (see, e.g., Fig. 6 B). Such kinks seem to result from defects within the MT bundle. These were included in the simulation by defining a defect position along the McTN as a finite region with significantly reduced bending rigidity. To compare the results in the presence and absence of the defect, the ratio of the wall connection was calculated (>1 if the relative wall connection is higher for a McTN with homogeneous bending, <1 otherwise). The effect of the defect site on the relative wall connection strongly depends on the position of the defect along the McTN and on its relative stiffness (Fig. 6 C). For low relative stiffness, the weak point minimally affects the wall connection ratio (Fig. 6 C, white colors). Only for stiff McTNs differences become visible. Thus, if the defect position is close to the cell body, the defect is rather disadvantageous for McTN-wall attachment (Fig. 6 C, red colors). In this case, two relatively straight pieces are energetically more favorable than a uniformly curved McTN, although the former leads to a weaker relative wall connection. If the defect position is at an intermediate position it also results in two pieces, but this time one tends to lay on the surface and thus creates a larger wall connection compared with the McTN with homogeneous bending (Fig. 6 C, light blue colors). If the defect position is close to the McTN tip there is only a small difference because the McTN is already aligned with the surface (see also Fig. S8 for more information on the McTN shape for different kink positions and relative stiffness). When the effect of all possible defect positions was averaged it became clear that such a defect is generally disadvantageous (Fig. 6 D). However, it should be noted that, for an accurate quantitative prediction of the effect of kinks on the overall shape of the McTN, the imposed stresses on the McTN and the actual form of the adhesive interaction need to be considered.

DISCUSSION

We used a combination of FRAP experiments and simulations to unravel the driving mechanism of McTN formation (Fig. 7 A). Since polymerization and sliding dynamics within McTNs occur on similar timescales, it is difficult to disentangle individual contributions in a noninvasive manner. Therefore, we used a theoretical model. This model takes into account the length dependence of MT tip dynamics as well as the dynamic load sharing between MTs both at the cell membrane. These are novel features for stochastic models of polymerization of biopolymers against soft barriers. With this model, we can predict the initiation of McTNs and the fluctuations in their length with very good agreement with our experimental data. A critical parameter in our model is the asymptotic force level F which determines McTN length (Fig. 4 B). The force depends on bending rigidity κ and surface tension σ of the cell membrane and on its adhesion w to the underlying actin cortex, given by $\mathcal{F} = 2\pi\sqrt{2\kappa(\sigma+w)}$ (47). Future experiments, such as AFM tether pulling experiments, are

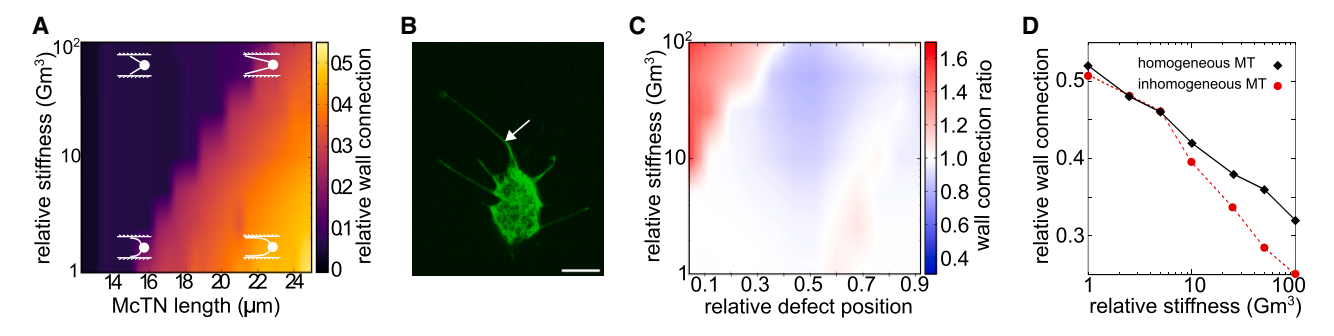


FIGURE 6 McTN adhesion to vessel walls. (A) Relative wall connection in terms of McTN length and relative stiffness of the McTN, E/ϵ (see text). (B) Example of a kink in a McTN of a kinesore-treated cell indicated by white arrow. Scale bar, 10 µm. (C) Ratio of the wall connection of a homogeneous McTN to that of a McTN with a kink in terms of the relative stiffness E/ϵ and the relative position of the kink with respect to the McTN tip. (D) Relative wall connection compared with the relative stiffness for filaments with homogeneous and inhomogeneous (i.e., with a kink) bending.

planned to investigate how these individual parameters are changed in CTCs to enable McTN growth. In our model, we found that both parameters, McTN length and curvature, are relevant for the adhesion strength to blood vessel walls. However, we have not yet included multiple McTNs in the current model. This will be interesting to study as multiple, long McTNs will compete for the available free membrane. The availability of free membrane influences surface tension, which in turn affects the force \mathcal{F} required to deform the membrane and initiate a protrusion. A reduction of free membrane limits membrane stretchability, thereby increasing surface tension and raising the force F. Future research should target the question whether few long McTNs or more and shorter McTNs are more favorable for facilitating adhesion to blood vessels. To answer the question of whether MT sliding dynamics also play a role in McTN formation, we included sliding dynamics in our theoretical model. While we could extract the parameters for MT polymerization dynamics from our EB3 experiments, we could not extract parameters for MT sliding dynamics. Despite taking several assumptions, such as setting the sliding velocity equal to polymerization velocity, our model allowed us to conclude that 1) there is MT sliding dynamics inside McTNs, 2) sliding dynamics plays a role on the timescale of fluorescent recovery, and 3) MT sliding hardly plays a role in generating McTNs. Our data from EB3 experiments suggest MT anchoring to the MTOC. However, direct evidence of MTOC anchoring was not possible. We note that also intermediate anchoring of MTs, for instance, at the position of the cell cortex, would lead to the same result: forces generated at the MT-bundle tip form the McTN and the reaction force exerted by the deformed membrane on the tip bends the McTN by pushing it against its anchorage point. Further, based on our theoretical model, we suggest that this curvature significantly enhances the ability of McTNs to attach to blood vessel walls. In this study of McTN curvature in blood vessels, we neglected the potential for McTN buckling. Our ongoing investigations indicate that the minimum force required for individual MT buckling is on the order of the force generated by a polymerizing MT. However, in a bundle of 10 MTs, the moment of inertia—and consequently the buckling force—increases by a factor of 100. This force far exceeds the membrane reaction forces at the McTN tip in response to MT polymerization. As a result, McTNs are unlikely to reach the buckling threshold and undergo abrupt shape changes, which is consistent with their slow, minor bending variations and predominantly straight shapes under minimal external stress in our experiments. In the bending-dominant regime, variations in filament stiffness result in gradual and smooth changes in filament shape, supporting the investigation of deformation-adhesion competition in our simulations. The combined effects of the inherent bending of McTNs, McTN-wall adhesion strength, and McTN length determine the extent of cell attachment to vessel walls (Fig. 7 B). We note that, for a more comprehensive study of the overall shape of the McTN interacting with vessel walls, the interplay of structural defects and imposed stresses on the McTN need to be considered. Recent studies have shown that the curvature and stability of MTs that experience mechanical stresses (such as when polymerizing against a membrane) are influenced by the induced lattice defects that yield in rescue sites along the MTs (74, 75). Molecular motors moving along MTs similarly induce lattice defects (76). The interplay of such defects and polymerization against a membrane affects the overall bending of the filament. In our experiments involving kinesore treatment, the role of MT sliding was more prominent. We provided evidence that this increased relevance of sliding coincides with MT detachment from the MTOC. Such detachment enhances the possible sliding distance of MTs in anterograde and retrograde directions. To our knowledge, how kinesore affects the anchorage in the MTOC has not been previously reported. The mechanism underlying this detachment remains speculative, but possibly the increased motor activity with this treatment affects the MT lattice to such an extent that it disconnects the MTs from the MTOC. Importantly, although the predominance of sliding in McTNs of kinesore-treated cells results in longer McTNs, these structures

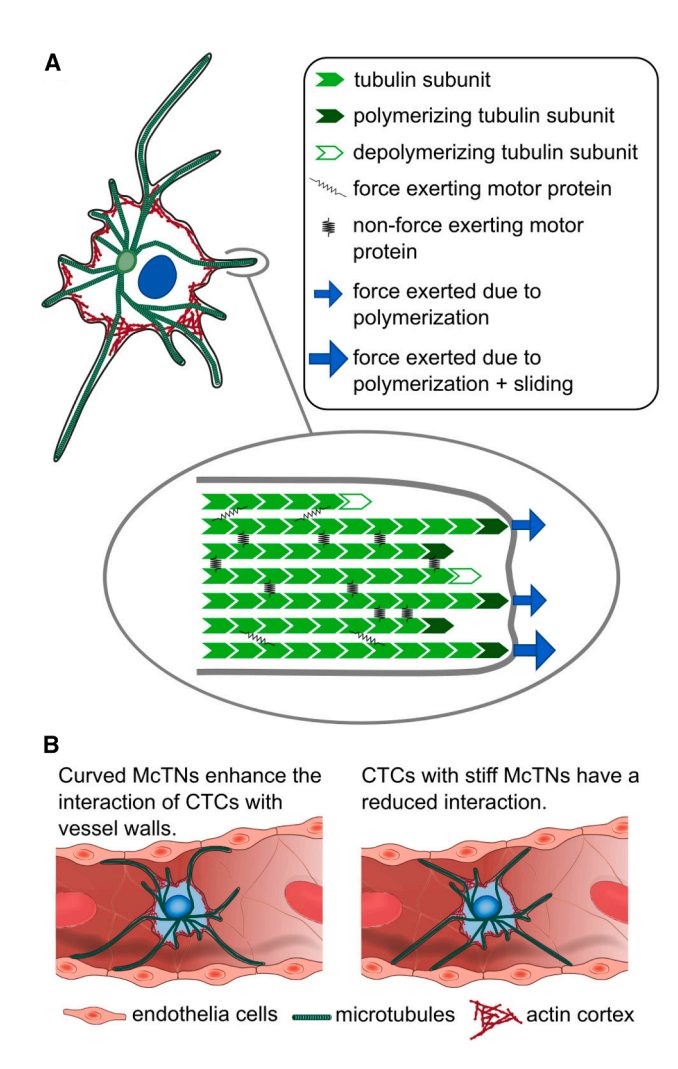


FIGURE 7 Scheme summarizing the mechanism of McTN formation and its function. (A) Polymerization of MTs drives McTN formation. The contribution of MT sliding powered by molecular motors is relatively weak. (B) Schematic representation of CTC within a blood vessel wall. Flexible McTN can enhance the contact with blood vessel walls and thus facilitate adhesion.

possibly contain kinks that may lead to reduced efficiency of adhesion to blood vessel walls. Our results show that the competition of elastic energy and general (nonspecific) adhesion determines the extent of cell attachment to vessel walls. This is in line with findings that active adhesion processes might not be critically involved in the process of extravasation. Instead, it depends on active processes that facilitate transendothelial migration (12). We propose that McTNs bring CTCs into close proximity with vessel walls through nonspecific interactions with walls, which potentially triggers downstream pathways and facilitates extravasation. Interaction with blood vessel walls is a critical step for CTC extravasation and metastasis formation. Future studies are planned to experimentally validate our findings from simulation using vasculature-mimicking systems and intravital microscopy. We suggest that length and bending of McTNs are key parameters to evaluate the metastatic potential of CTCs and should be considered when designing novel therapeutic strategies.

ACKNOWLEDGMENTS

This work was funded by the Deutsche Forschungsgemeinschaft (DFG) via Collaborative Research Center 1027. R.S. acknowledges support by the Young Investigator Grant of Saarland University, grant no. 7410110401. We thank Rhoda J. Hawkins (AIMS Ghana, University of Sheffield), Stefan Diez (TU Dresden), Kristian Franze (Institute for Medical Physics, Friedrich-Alexander-Universität Erlangen-Nürnberg, Erlangen, Germany), and Laura Aradilla Zapata (née Schaedel, Saarland University) for fruitful discussions.

AUTHOR CONTRIBUTIONS

F.L., R.S., and L.S. designed the study. F.L. and L.K. designed the experiments. L.K. and K.K. performed the experiments. R.S. and L.S. developed the model. R.S. and J.B. performed the simulations. L.K. and R.S. analyzed the data. All of the authors contributed to the interpretation of the results. L. K. and R.S. wrote the manuscript.

DECLARATION OF INTERESTS

The authors declare no competing interests.

DECLARATION OF GENERATIVE AI AND AI-ASSISTED TECHNOLOGIES IN THE WRITING **PROCESS**

During the preparation of this work the authors used ChatGPT 3 (OpenAI) to improve readability and language. After using this tool/service, the authors reviewed and edited the content as needed and take full responsibility for the content of the publication.

SUPPORTING MATERIAL

Supporting material can be found online at https://doi.org/10.1016/j.bpj. 2025.05.018.

SUPPORTING CITATIONS

Reference (77) appears in the supporting material.

REFERENCES

- 1. Alix-Panabières, C., and K. Pantel. 2014. Challenges in circulating tumour cell research. Nat. Rev. Cancer. 14:623-631.
- 2. Pantel, K., and M. R. Speicher. 2016. The biology of circulating tumor cells. Oncogene. 35:1216-1224.
- 3. Hamza, B., S. R. Ng, ..., S. R. Manalis. 2019. Optofluidic real-time cell sorter for longitudinal CTC studies in mouse models of cancer. Proc. Natl. Acad. Sci. USA. 116:2232-2236.
- 4. Vermesh, O., A. Aalipour, ..., S. S. Gambhir. 2018. An intravascular magnetic wire for the high-throughput retrieval of circulating tumour cells in vivo. Nat. Biomed. Eng. 2:696-705.
- 5. Ting, D. T., B. S. Wittner, ..., D. A. Haber. 2014. Single-cell RNA sequencing identifies extracellular matrix gene expression by pancreatic circulating tumor cells. Cell Rep. 8:1905-1918.

- Miyamoto, D. T., Y. Zheng, ..., D. A. Haber. 2015. RNA-Seq of single prostate CTCs implicates noncanonical Wnt signaling in antiandrogen resistance. Sci. Technol. Humanit. 349:1351–1356.
- Aceto, N., A. Bardia, ..., S. Maheswaran. 2014. Circulating tumor cell clusters are oligoclonal precursors of breast cancer metastasis. *Cell*. 158:1110–1122.
- Au, S. H., B. D. Storey, ..., M. Toner. 2016. Clusters of circulating tumor cells traverse capillary-sized vessels. *Proc. Natl. Acad. Sci. USA*. 113:4947–4952.
- Sarioglu, A. F., N. Aceto, ..., M. Toner. 2015. A microfluidic device for label-free, physical capture of circulating tumor cell clusters. *Nat. Methods*. 12:685–691.
- Chambers, A. F., A. C. Groom, and I. C. MacDonald. 2002. Dissemination and growth of cancer cells in metastatic sites. *Nat. Rev. Cancer*. 2:563–572.
- Massagué, J., and A. C. Obenauf. 2016. Metastatic colonization by circulating tumour cells. *Nature*. 529:298–306.
- Strilic, B., and S. Offermanns. 2017. Intravascular Survival and Extravasation of Tumor Cells. Cancer Cell. 32:282–293.
- Whipple, R. A., A. M. Cheung, and S. S. Martin. 2007. Detyrosinated microtubule protrusions in suspended mammary epithelial cells promote reattachment. *Exp. Cell Res.* 313:1326–1336.
- Balzer, E. M., R. A. Whipple, ..., S. S. Martin. 2010. Antimitotic chemotherapeutics promote adhesive responses in detached and circulating tumor cells. *Breast Cancer Res. Treat.* 121:65–78.
- Boggs, A. E., M. I. Vitolo, ..., S. S. Martin. 2015. alpha-Tubulin acetylation elevated in metastatic and basal-like breast cancer cells promotes microtentacle formation, adhesion, and invasive migration. *Cancer Res.* 75:203–215.
- Matrone, M. A., R. A. Whipple, ..., S. S. Martin. 2010. Metastatic breast tumors express increased tau, which promotes microtentacle formation and the reattachment of detached breast tumor cells. *Oncogene*. 29:3217–3227.
- Whipple, R. A., M. A. Matrone, ..., S. S. Martin. 2010. Epithelial-to-mesenchymal transition promotes tubulin detyrosination and microtentacles that enhance endothelial engagement. *Cancer Res.* 70:8127–8137.
- Korb, T., K. Schlüter, ..., J. Haier. 2004. Integrity of actin fibers and microtubules influences metastatic tumor cell adhesion. *Exp. Cell Res*. 299:236–247.
- Bouchet, B. P., and A. Akhmanova. 2017. Microtubules in 3D cell motility. J. Cell Sci. 130:39–50.
- Etienne-Manneville, S. 2013. Microtubules in Cell Migration. Annu. Rev. Cell Dev. Biol. 29:471–499.
- Yamada, K. M., and M. Sixt. 2019. Mechanisms of 3D cell migration. Nat. Rev. Mol. Cell Biol. 20:738–752.
- Caswell, P. T., and T. Zech. 2018. Actin-Based Cell Protrusion in a 3D Matrix. Trends Cell Biol. 28:823–834.
- Laughlin, S. B., and T. J. Sejnowski. 2003. Communication in Neuronal Networks. Science. 301:1870–1874.
- Buszczak, M., M. Inaba, and Y. M. Yamashita. 2016. Signaling by Cellular Protrusions: Keeping the Conversation Private. *Trends Cell Biol.* 26:526–534.
- Mattila, P. K., and P. Lappalainen. 2008. Filopodia: molecular architecture and cellular functions. *Nat. Rev. Mol. Cell Biol.* 9:446–454.
- Marshall, W. F., and S. Nonaka. 2006. Cilia: Tuning in to the Cell's Antenna. Curr. Biol. 16:R604–R614.
- Le Clainche, C., and M.-F. Carlier. 2008. Regulation of Actin Assembly Associated With Protrusion and Adhesion in Cell Migration. *Physiol. Rev.* 88:489–513.
- Linder, S., P. Cervero, ..., J. Condeelis. 2023. Mechanisms and roles of podosomes and invadopodia. *Nat. Rev. Mol. Cell Biol.* 24:86–106.
- Bender, M., J. N. Thon, ..., J. H. Hartwig. 2015. Microtubule sliding drives proplatelet elongation and is dependent on cytoplasmic dynein. *Blood*. 125:860–868.

- Lu, W., P. Fox, ..., V. I. Gelfand. 2013. Initial Neurite Outgrowth in Drosophila Neurons Is Driven by Kinesin-Powered Microtubule Sliding. Curr. Biol. 23:1018–1023.
- 31. Peskin, C. S., G. M. Odell, and G. F. Oster. 1993. Cellular motions and thermal fluctuations: the Brownian ratchet. *Biophys. J.* 65:316–324.
- 32. Theriot, J. A. 2000. The Polymerization Motor. Traffic. 1:19-28.
- Jakobs, M., K. Franze, and A. Zemel. 2015. Force generation by molecular-motor-powered microtubule bundles; implications for neuronal polarization and growth. Front. Cell. Neurosci. 9:441.
- Oelz, D. B., U. Del Castillo, ..., A. Mogilner. 2018. Microtubule Dynamics, Kinesin-1 Sliding, and Dynein Action Drive Growth of Cell Processes. *Biophys. J.* 115:1614–1624.
- Lu, W., M. Lakonishok, and V. I. Gelfand. 2015. Kinesin-1-powered microtubule sliding initiates axonal regeneration in Drosophila cultured neurons. *Mol. Biol. Cell.* 26:1296–1307.
- Fygenson, D. K., J. F. Marko, and A. Libchaber. 1997. Mechanics of Microtubule-Based Membrane Extension. *Phys. Rev. Lett.* 79:4497–4500.
- Emsellem, V., O. Cardoso, and P. Tabeling. 1998. Vesicle deformation by microtubules: A phase diagram. *Phys. Rev. E.* 58:4807–4810.
- 38. Gavriljuk, K., B. Scocozza, ..., P. I. H. Bastiaens. 2021. A self-organized synthetic morphogenic liposome responds with shape changes to local light cues. *Nat. Commun.* 12:1548.
- Bouchet, B. P., I. Noordstra, ..., A. Akhmanova. 2016. Mesenchymal Cell Invasion Requires Cooperative Regulation of Persistent Microtubule Growth by SLAIN2 and CLASP1. Dev. Cell. 39:708–723.
- Jakobs, M. A. H., A. Dimitracopoulos, and K. Franze. 2019. KymoButler, a deep learning software for automated kymograph analysis. *eLife*. 8:e42288.
- Fritzsche, M., and G. Charras. 2015. Dissecting protein reaction dynamics in living cells by fluorescence recovery after photobleaching. Nat. Protoc. 10:660–680.
- 42. Dogterom, M., and S. Leibler. 1993. Physical aspects of the growth and regulation of microtubule structures. *Phys. Rev. Lett.* 70:1347–1350.
- 43. Ebbinghaus, M., and L. Santen. 2011. Theoretical modeling of aging effects in microtubule dynamics. *Biophys. J.* 100:832–838.
- 44. Antal, T., P. L. Krapivsky, ..., B. Chakraborty. 2007. Dynamics of an idealized model of microtubule growth and catastrophe. *Phys. Rev. E*, 76:041907.
- Derényi, I., F. Jülicher, and J. Prost. 2002. Formation and interaction of membrane tubes. *Phys. Rev. Lett.* 88:238101.
- Powers, T. R., G. Huber, and R. E. Goldstein. 2002. Fluid-membrane tethers: Minimal surfaces and elastic boundary layers. *Phys. Rev. E*. 65:041901.
- Sheetz, M. P. 2001. Cell control by membrane–cytoskeleton adhesion. Nat. Rev. Mol. Cell Biol. 2:392–396.
- 48. Dogterom, M., M. E. Janson, ..., B. M. Mulder. 2002. Force generation by polymerizing microtubules. *Appl. Phys. A*. 75:331–336.
- Stukalin, E. B., and A. B. Kolomeisky. 2004. Simple growth models of rigid multifilament biopolymers. J. Chem. Phys. 121:1097–1104.
- Janson, M. E., M. E. de Dood, and M. Dogterom. 2003. Dynamic instability of microtubules is regulated by force. *J. Cell Biol*. 161:1029–1034.
- Foethke, D., T. Makushok, ..., F. Nédélec. 2009. Force- and lengthdependent catastrophe activities explain interphase microtubule organization in fission yeast. *Mol. Syst. Biol.* 5:241.
- Govindan, B. S., and W. B. Spillman. 2004. Steady states of a microtubule assembly in a confined geometry. *Phys. Rev. E*. 70:032901.
- Weber, I., C. Appert-Rolland, ..., L. Santen. 2018. Non-equilibrium fluctuations of a semi-flexible filament driven by active cross-linkers. *Europhys. Lett.* 120:38006.
- Kratky, O., and G. Porod. 1949. Röntgenuntersuchung gelöster Fadenmoleküle. Recl. Trav. Chim. Pays. Bas. 68:1106–1122.

- 55. Camalet, S., and F. Jülicher. 2000. Generic aspects of axonemal beating. *New J. Phys.* 2:324.
- Vardas, V., J. A. Ju, ..., G. Kallergi. 2023. Functional Analysis of Viable Circulating Tumor Cells from Triple-Negative Breast Cancer Patients Using TetherChip Technology. Cells. 12:1940.
- Matrone, M. A., R. A. Whipple, ..., S. S. Martin. 2010. Microtentacles tip the balance of cytoskeletal forces in circulating tumor cells. *Cancer Res.* 70:7737–7741.
- Killilea, A. N., R. Csencsits, ..., K. H. Downing. 2017. Cytoskeletal organization in microtentacles. Exp. Cell Res. 357:291–298.
- Kapitein, L. C., and C. C. Hoogenraad. 2015. Building the Neuronal Microtubule Cytoskeleton. *Neuron (Camb., Mass.)*. 87:492–506.
- 60. Hartwig, J., and J. Italiano. 2003. The birth of the platelet. *J. Thromb. Haemost.* 1:1580–1586.
- Italiano, J. E., Jr., P. Lecine, ..., J. H. Hartwig. 1999. Blood Platelets Are Assembled Principally at the Ends of Proplatelet Processes Produced by Differentiated Megakaryocytes. J. Cell Biol. 147:1299–1312.
- Dallon, J. C., C. Leduc, ..., S. Portet. 2022. Using Fluorescence Recovery After Photobleaching data to uncover filament dynamics. *PLoS Comput. Biol.* 18:e1010573.
- Jolly, A. L., H. Kim, ..., V. I. Gelfand. 2010. Kinesin-1 heavy chain mediates microtubule sliding to drive changes in cell shape. *Proc. Natl. Acad. Sci. USA*. 107:12151–12156.
- 64. Randall, T. S., Y. Y. Yip, ..., M. P. Dodding. 2017. A small-molecule activator of kinesin-1 drives remodeling of the microtubule network. *Proc. Natl. Acad. Sci. USA*. 114:13738–13743.
- Shaebani, M. R., A. Pasula, ..., L. Santen. 2016. Tracking of plus-ends reveals microtubule functional diversity in different cell types. Sci. Rep. 6:30285.

- Shaebani, M. R., A. Wysocki, ..., H. Rieger. 2020. Computational Models for Active Matter. Nat. Rev. Phys. 2:181–199.
- Laan, L., J. Husson, ..., M. Dogterom. 2008. Force-generation and dynamic instability of microtubule bundles. *Proc. Natl. Acad. Sci. USA*. 105:8920–8925.
- 68. van Doorn, G. S., C. Tanase, ..., M. Dogterom. 2000. On the stall force for growing microtubules. *Eur. Biophys. J.* 29:2–6.
- Krawczyk, J., and J. Kierfeld. 2011. Stall force of polymerizing microtubules and filament bundles. *Europhys. Lett.* 93:28006.
- Berezuk, M. A., and T. A. Schroer. 2004. Fractionation and Characterization of Kinesin II Species in Vertebrate Brain. *Traffic*. 5:503–513.
- Kerssemakers, J., J. Howard, ..., S. Diez. 2006. The distance that kinesin-1 holds its cargo from the microtubule surface measured by fluorescence interference contrast microscopy. *Proc. Natl. Acad. Sci. USA*. 103:15812–15817.
- Akhmanova, A., and L. C. Kapitein. 2022. Mechanisms of microtubule organization in differentiated animal cells. *Nat. Rev. Mol. Cell Biol.* 23:541–558.
- Butt, H., K. Graf, and M. Kappl. 2003. Physics and Chemistry of Interfaces. Wiley-VCH Verlag Co, Weinheim, Germany.
- Li, Y., O. Kučera, ..., M. Théry. 2023. Compressive forces stabilize microtubules in living cells. *Nat. Mater.* 22:913–924.
- Schaedel, L., K. John, ..., M. Théry. 2015. Microtubules self-repair in response to mechanical stress. *Nat. Mater.* 14:1156–1163.
- Triclin, S., D. Inoue, ..., M. Théry. 2021. Self-repair protects microtubules from destruction by molecular motors. *Nat. Mater.* 20:883–891.
- Chugh, P., A. G. Clark, ..., E. K. Paluch. 2017. Actin cortex architecture regulates cell surface tension. *Nat. Cell Biol.* 19:689–697.